



HAL
open science

All-magnetic slabs and Multiferroism in (Bi_{2-x}O₂)(MF₄) Aurivillius oxyfluorides, (M= Fe, Ni)

Olivier Mentré, Miguel A Juárez-Rosete, Marie Colmont, Clemens Ritter,
François Fauth, Mathieu Duttine, Marielle Huvé, Christine Terryn, Victor
Duffort, Angel Arévalo-López

► **To cite this version:**

Olivier Mentré, Miguel A Juárez-Rosete, Marie Colmont, Clemens Ritter, François Fauth, et al.. All-magnetic slabs and Multiferroism in (Bi_{2-x}O₂)(MF₄) Aurivillius oxyfluorides, (M= Fe, Ni). Chemistry of Materials, 2022, 34 (12), pp.5706-5716. 10.1021/acs.chemmater.2c01213 . hal-03783310

HAL Id: hal-03783310

<https://hal.science/hal-03783310v1>

Submitted on 22 Sep 2022

HAL is a multi-disciplinary open access archive for the deposit and dissemination of scientific research documents, whether they are published or not. The documents may come from teaching and research institutions in France or abroad, or from public or private research centers.

L'archive ouverte pluridisciplinaire **HAL**, est destinée au dépôt et à la diffusion de documents scientifiques de niveau recherche, publiés ou non, émanant des établissements d'enseignement et de recherche français ou étrangers, des laboratoires publics ou privés.

All-magnetic slabs and Multiferroism in $(\text{Bi}_{2-x}\text{O}_2)(\text{MF}_4)$ Aurivillius oxyfluorides, (M= Fe, Ni).

Olivier Mentre^{1,*}, Miguel A. Juárez-Rosete¹, Marie Colmont¹, Clemens Ritter², François Fauth³, Mathieu Duttine⁴, Marielle Huvé¹, Christine Terryn⁶, Victor Duffort¹, Ángel M. Arévalo-López¹.

1) *Université Lille, CNRS, Centrale Lille, Université Artois, UMR 8181, UCCS, Unité de Catalyse et Chimie du Solide, F-59000 Lille, France*

2) *Institut Laue-Langevin, 71 Avenue des Martyrs, 38042 Grenoble, Cedex, France*

3) *CELLS-ALBA Synchrotron, Cerdanyola del Vallès, Barcelona E-08290, Spain*

4) *CNRS, Université de Bordeaux, Bordeaux INP, ICMCB, UMR 5026, F-33600 Pessac, France*

5) *Institut Michel-Eugene Chevreul - FR 2638, Université de Lille, France*

6) *Université de Reims Champagne Ardenne, PICT, Plateforme Imagerie Cellulaire et Tissulaire, 51 Rue Cognacq-Jay, 51100 Reims, France*

* Corresponding author, email : Olivier.mentre@univ-lille.fr

Abstract

The Aurivillius layered compounds with predominant fraction of paramagnetic transition metals are an emerging playground for discovery of magnetoelectric or multiferroic compounds. This aim was recently achieved by incorporating F⁻ anions in the perovskite layer of the $(\text{Bi}_2\text{O}_2)(\text{CoF}_4)$ compound, only described so-far in a disordered model (unit cell : a_p, a_p, c). Here we report the investigation on the representative compounds $(\text{Bi}_2\text{O}_2)(\text{MF}_4)$ (M = Fe, Ni) using single crystal, synchrotron, neutron and electron diffraction. These reveal that the crystallographic average cell ($\sqrt{2}x a_p, \sqrt{2}x a_p, c$) is orthorhombic, polar and accompanied by versatile (in)commensurate modulations. The supercell model was fully refined for $(\text{Bi}_{2-x}\text{O}_2)(\text{FeF}_4)$ ($q = (0, \frac{1}{2}, 0)$) in the $P2_111$ polar space group with transverse Fe-displacements relative to q . Bi-deficiency is compensated by a mixed Fe^{-2.5+} valence, but, the ideal stoichiometry is preserved for $(\text{Bi}_2\text{O}_2)(\text{NiF}_4)$. Both compounds are antiferromagnetic below $T_N = 89$ K (Fe) and 45 K (Ni) with moments lying in the (ac) plane and a weak ferromagnetic component along the b -axis. DFT calculations validate a strongly anisotropic distribution of magnetic exchanges ($J_{ab}/J_c > 10$). A broad anomaly on the dielectric constant at T_N and a polarization loop at room temperature were obtained on $(\text{Bi}_{2-x}\text{O}_2)(\text{FeF}_4)$ single crystals, revealing multiferroism with magneto electric couplings.

1. Introduction

The *Aurivillius* series of compounds with formula $(\text{Bi}_2\text{O}_2)(\text{A}_{n-1}\text{B}_n\text{O}_{3n+1})$ contains perovskite blocks of variable thicknesses, $n = 1, 2, 3 \dots$ separated by Bi/O slabs, where A is 12-coordinated, and B is a 6-coordinated transition metal^[1]. Apart from partial substitutions, the B sites are commonly limited to diamagnetic cations in high oxidation states (Ti^{4+} , Nb^{5+} , Ta^{5+} , $\text{W}^{6+} \dots$). The combination of the Bi^{3+} lone pair effect in its 2D fluorite slab along with the 2nd order Jahn-Teller effect of the d^0 B cation result in polar phases and make these *Aurivillius* compounds an important class of ferroelectric oxides^[2], as for instance $(\text{Bi}_2\text{O}_2)(\text{Bi}_2\text{Ti}_3\text{O}_{10})$ which is used as high temperature acoustic piezo-sensor^[3]. The incorporation of cations with partially occupied d^n states into the perovskite slab will then work as a platform for the further development of multiferroic magnetoelectrics. However, these cations would generally require low oxidation states compared to the above *Aurivillius* standards. Besides the preparation difficulties, an extra challenge for the synthesis of new multiferroics is that the main mechanism based on 2nd order Jahn-Teller effect for creating a proper polar instability is disfavored by the partially occupied valence shell of d^n ions^[4]. Thus the role of Bi^{3+} on the structural instability is crucial, as in the prototypical multiferroic BiFeO_3 ^[5]. Following this idea, theoretical multiferroic perspectives have been explored for Fe^{3+} -substituted *Aurivillius* phases such as the $n = 4$ $(\text{Bi}_2\text{O}_2)(\text{Bi}_3\text{FeTi}_3\text{O}_{13})$, but remain controversial due to conflicting magnetic measurements^[6], and suggest sample-dependent properties due to varying degree of $\text{Fe}^{3+}/\text{Ti}^{4+}$ ordering.

An alternative way to efficiently incorporate large concentration of magnetically-active $3d$ transition metal cations is to partially substitute O^{2-} by F^- in the preferred perovskite sublattice. Besides the limited number of bismuth-based diamagnetic oxyfluorides reported such as $(\text{Bi}_2\text{O}_2)(\text{BiTi}^{4+}_2\text{O}_6\text{F})$ ^[7], $(\text{Bi}_2\text{O}_2)(\text{Ti}^{4+}\text{O}_2\text{F}_2)$ ^[8], and $(\text{Bi}_2\text{O}_2)(\text{V}^{4.7+}\text{O}_3\text{F}_{0.7})$ ^[9] the recent synthesis of the *Aurivillius* compound ($n = 1$) $(\text{Bi}_2\text{O}_2)(\text{Co}^{2+}\text{F}_4)$ opens wide potentialities to combine polar and magnetic orders into new multiferroics with relevant transition metal ions^[10]. $(\text{Bi}_2\text{O}_2)(\text{Co}^{2+}\text{F}_4)$ shows antiferromagnetic ordering below $T_N \sim 50$ K and develops a weak spontaneous magnetization. Single crystal X-ray diffraction (XRD) data were refined in a disordered $I-4$ space group, with a four-fold splitting of all axial and equatorial F^- positions. This disorder allowed the authors to propose layers of tilted CoF_6 . Such ambiguities are reminiscent of possible O/F mixed occupancies and requires the use of accurate complementary techniques in order to dissipate them. For instance, the combination of synchrotron X ray powder diffraction (SXRPD), neutron powder diffraction (NPD) and second harmonic

generation (SHG) test applied to $(\text{Bi}_2\text{O}_2)(\text{NbO}_3\text{F})$, returned the non-polar $Pbca$ space group with preferential occupancy of the apical perovskite positions by F^- anions ^[11]. On the other hand, in $(\text{Bi}_2\text{O}_2)(\text{TiO}_2\text{F}_2)$, there is still no clear consensus on the real O/F distribution over equatorial and axial anion positions. A first experimental work reported bulk-ferroelectricity around 284 K ^[12] while a non-polar space group with F^- in the equatorial position was suggested from a combined XRD-PND study ^[8]. More recently, the O/F ordering in $(\text{Bi}_2\text{O}_2)(\text{TiO}_2\text{F}_2)$ was deeply re-investigated as a crucial parameter for tuning the symmetry, and to break or not the inversion center. However, even powerful tools such as the symmetry analysis combined with i) Rietveld and strain analysis ^[13] or with ii) energetic metastability by first principle calculations ^[14] offer a nice energetic and configurational panorama but do not allow for a clear discrimination between multiple O/F ordering possibilities. Altogether, these results highlight the major obstacles against a robust structural analysis of *Aurivillius* oxyfluorides, even in divalent cation cases (Co^{2+}) where the ideal $(\text{Bi}_2\text{O}_2)(\text{CoF}_4)$ may be affected by triple O – F – □ substitution (□ : anion vacancy).

Here we present the novel compounds $(\text{Bi}_{2-x}\text{O}_2)(\text{MF}_4)$ $M = \text{Fe}$ and Ni . In the case of $(\text{Bi}_{2-x}\text{O}_2)(\text{FeF}_4)$, also referred as BiFeOF in this article, the structural ambiguities have been unraveled combining single crystal, powder XRD and NPD, Second Harmonic Generation (SHG), (Scanning) Transmission Electron Microscopy (STEM-TEM), Mössbauer spectroscopy and DFT-calculations. Our structural conclusions have been consistently applied to the $(\text{Bi}_2\text{O}_2)(\text{NiF}_4)$ case, referred as BiNiOF. The main magneto-electric properties are discussed leading to the discovery of a new series of multiferroic materials.

2. Single crystal XRD Crystal Structure of $(\text{Bi}_{2-x}\text{O}_2)(\text{FeF}_4)$

Single crystal XRD of $(\text{Bi}_{2-x}\text{O}_2)(\text{FeF}_4)$ displays the typical *Aurivillius* phase reflexions with an average pseudo-tetragonal ($a = \sqrt{2}x a_p$, $b = \sqrt{2}x a_p$, c) unit-cell commonly observed due to octahedral tilts. Here a_p refers to the perovskite based subcell ($a_p \sim 3.8 \text{ \AA}$, $c \sim 16.5 \text{ \AA}$). Comparison of the $[hk1]$ precession frames of two different collected crystals with different ratio of pseudo-tetragonal twin fractions evidence a doubling of a single basal lattice parameter only, see Figure 1a-b. Thus, the extra peaks can be associated to a $(a, 2xb, c)$ orthorhombic supercell as shown in Figure 1. Long XRD collection times were required in order to observe the $2xb$ weak supercell spots by XRD. The b -doubling is highlighted in the $[100]$ electron diffraction patterns as shown by blue arrows in Figure 1c.

2.1. Polar average Structure: Analysis of the systematic extinctions of the fundamental diffracted reflections, for the less twinned crystal agreed to those deduced from ED patterns, see Figures 1c and 1d. In the $a=b\sim 5.4 \text{ \AA}$, $c\sim 16.5 \text{ \AA}$ subcell, weak $0kl$ ($l=2n+1$) peaks refute the orthorhombic $Pcab$ centrosymmetric (CS) space group, but agree well with the polar $P2_1ab$ one. At this stage it is noteworthy that the CS $Pcab$ is not considered in the subgroup list of the parent ideal $I4/mmm$ for any F / O distribution in $[\text{Bi}_2\text{O}_2][\text{TiO}_2\text{F}_2]$ ^[14], while our symmetry analysis shows its relevance, see Fig. S1. It results from applying X2+ and X3+ distortions to the $I4/mmm$ parent group. Note on the Figure 1c, that the $0k0:k = 2n+1$ and $00l:l = 2n+1$ spots (highlighted in green) are generated by ED multiple diffraction phenomena. The obtained model is reminiscent of the room-temperature ferroelectric form of $(\text{Bi}_2\text{O}_2)(\text{WO}_4)$ ^[15] and $(\text{Bi}_2\text{O}_2)(\text{MoO}_4)$ ^[16], previously determined by NPD ^[17]. Indeed, although the well-known Glazer notation ^[18] for rotations in perovskites is not completely adapted to the layered *Aurivillius* $n = 1$ phase, our model corresponds to an a^-a^- in plane rotation with an *in-phase* rotation along the c axis in between disconnected FeF_6 octahedra layers. The polar $P2_1ab$ space group hypothesis is supported by the detection of SHG signal (21 mW laser-power) on crystals. A strong influence of the crystal quality and orientation on the SHG emission exists, and only misoriented crystals towards the vertical laser beam, or the $[110]$ planes of well-aligned ones emit, see Figures 1e and S1. At this stage, the refinement in the subcell also reveals weak Fe displacements in the equatorial plane towards an octahedral edge along the polar 2_1 -axis. due to large Fe thermal parameters and Fourier difference peaks suggest Fe splitting over two off-centered position $\text{Fe}_a\text{-Fe}_b$, which improves the convergence by $\sim 0.5\%$ ($R_{obs} = 4.84\%$) and returns reasonable U thermal parameter values of $\sim 0.07 \text{ \AA}^2$ for both Fe sites. The amplitude of the split is weak ($d(\text{Fe}_a\text{-Fe}_b) = 0.18 \text{ \AA}$) but its ordering along the b -axis may stand as the main ingredient for the b -axis doubling, as treated in the next section

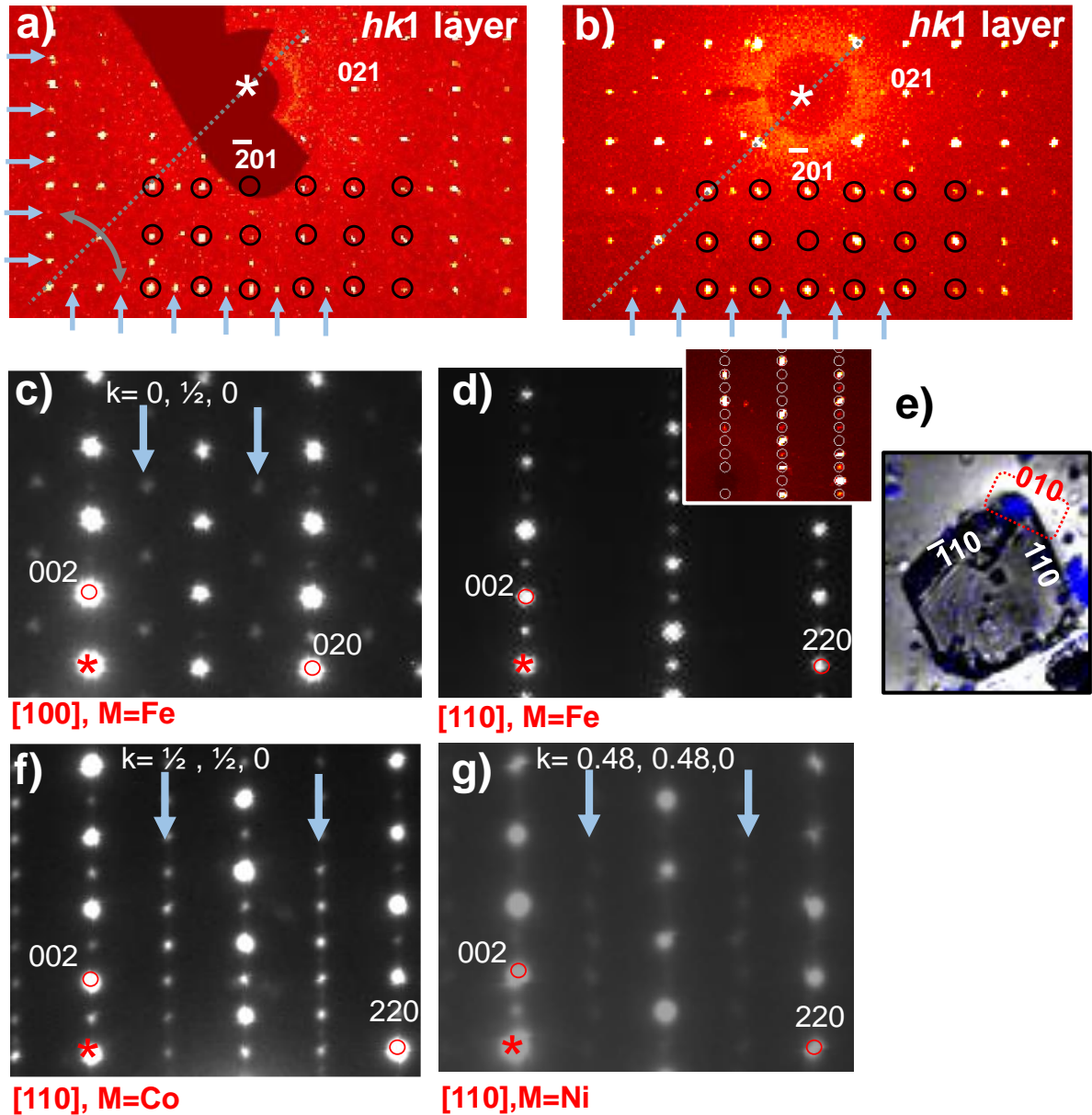


Figure 1: a,b) $hk1$ XRD-reconstructed precession frames for two BiFeOF single crystals with different pseudo-tetragonal twin ratio. The black circles show evidence of the b-doubling. c,d) BiFeOF : [100] and [110] electron diffraction zone axis patterns (EDZAP). Blue arrows show the modulation spots and green squares show spots created by multi-diffraction phenomena. e) Transmission and SHG (blue) images of a BiFeOF crystals with highlight of the emitting (010) truncated face. f,g) [110] EDZAP for BCoOF and BiNiOF with evidence of superstructure phenomena.

2.2. Supercell 4D approach: Here, we investigate the origin of the b-doubling using a super space 4D-formalism, in which displacive modulation assigned to atoms enhance the contributions of the weak $(0, \frac{1}{2}, 0)$ satellites compared to the intense fundamental peaks. The two possible super space groups (SSG) compatible with the P_{21ab} symmetry are $P_{21ab}(0\frac{1}{2}0)000$ and $P_{21ab}(0\frac{1}{2}0)00s$. However, due to the weak satellite intensities, they were undistinguishable by extinction conditions involving the $(hklm)$ m 4th index. The former SSG returns the best

satellite agreement with $R_{sat.} = 26.05\%$ after modulation of the Fe position by a smooth 1st order string. This is further lowered to $R_{sat.} = 22.5\%$ by adding modulated Bi positions. In essence it validates the effective Fe splitting as shown by black arrows on the Figure 2a showing the 4D Fourier-map around the Fe position with significant super-periodic Δx off-centering. Finally, the influence of anionic modulation waves on the agreement factors is very modest in this model, due to the monoclinic symmetry detailed below. We did not push the 4D model in a modulated monoclinic symmetry because the number of refined parameters is very similar to a standard 3D-treatment in the super cell.

2.3. Supercell final model and Bi-deficiency: A robust 3D-model with refined anionic local coordinates was reached in the $(a, 2b, c)$ supercell using approximately the same number of refined parameters as for the prior 4D-refinement. Group-theory analysis using *Isosubgroup* with the $(0, \frac{1}{2}, 0)$ q vector over the $P2_1ab$ space group, leads to the monoclinic $Pa11$ or $P2_111$ solutions, the latter agreeing with the commensurate supercell group of the select SSG. Only the $P2_111$ solution leads to a consistent model, with $R_{obs} = 5.40\%$ using a unit weighting scheme, due to the large number of weak supercell spots. This model preserves the Fe split along the a -axis (black arrows on Fig. 2e) described previously, and overall a cooperative polar displacement of Fe in their F_6 octahedra occurs along the polar a -axis (white arrows on Fig.2e). The refinement of the Bi occupancies (each of the 8 independent positions being constrained equally occupied) results in the $(Bi_{1.8}O_2)FeO_2F_4$ formula with $R_{obs} = 5.1\%$. This behavior is similar to the one observed in $(Bi_{2-x}O_2)(V_2O_{11-y})$, found to tolerate a large number of Bi vacancies without breaking the high temperature prototype.^[19] A collection of crystallographic data, positional, BVS, thermal parameters and inter atomic distances are listed in S.I, Tables S1-S4, Supporting Information. The bond valence sums (BVS) calculated for all 16 independent F^- anions located on the perovskite octahedra range in between -0.76 and -1.02 , while those calculated for oxygen in the fluorite $[Bi_2O_2]$ blocks are in between -2.1 and -2.2 and comfort an ideal anion ordering. This is also consistent with the O/F ratio of 0.505 found by EDS.

The BVS for the four independent Fe anions ($1.88 < d(Fe-F) < 2.20 \text{ \AA}$) lead to values between $+2.6$ and $+3.0$, in good agreement with the mixed iron valent state. However, despite the displacement of the Fe ions in the a -direction along the superstructure axis discussed above, charge ordering is not clear. To the best of our knowledge, the $(Bi_{2-x}O_2)(FeF_4)$ crystal structure

is a unique case of 2D $[\text{FeF}_4]$ lattice with strong contraction of the Fe-F bonds due to bidentate F⁻ position (Fe – F – Fe $\sim 180^\circ$). It is not representative of ferrous 3D architectures, *e.g.* rutile FeF_2 or perovskite KFeF_3 , from which the BVS parameters have been deduced. The refined model with octahedral tilts is shown in Figures 2b and 2c. The high-angle annular dark field (HAADF) stem image shown in Figure 2d shows the absence of stacking faults on large domains but did not allow to observe local Bi-vacancies, due to the projection over tens of cells.

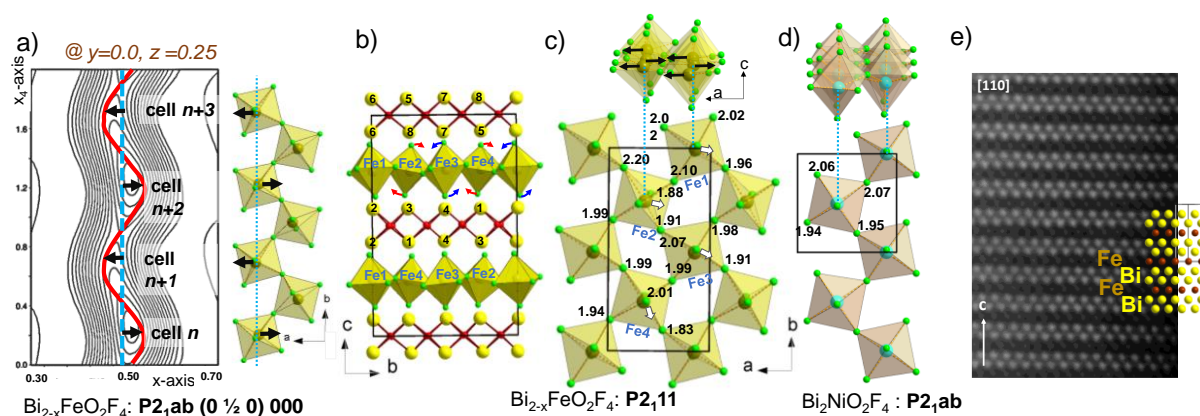


Figure 2 : a) BiFeOF : 4D approach : $(x, x4)$ Fourier section around the Fe position (summed 1 Å in y and z). The red line corresponds to the refined displacive wave around the central position (blue line) with the corresponding structural model (right). b) Projected structure in the (b, c) plane with evidences of the octahedral tilt around the c -axis. c) Projected perovskite slab in the (b, c) plane with main Fe sheets along the a -axis (black arrows) and ferroelectric displacements in the FeF_6 octahedra (white arrows). d) BiFeOF $[110]$ HAADF STEM image where the contrast is proportional to z^2 , *i.e.* heavy atoms are brighter. e) BiNiOF perovskite slab

3. Mössbauer spectroscopy and powder diffraction.

The best samples (polycrystalline and single crystals) were prepared in stoichiometric 2:1 Bi:Fe conditions, after sonication and separation cycles in order to remove impurities. The sample contains byproducts in addition to the main $\text{Bi}_2\text{FeO}_2\text{F}_4$ ($\sim 80(1)$ w%) phase, *i.e.* BiF_3 ($\sim 1.8(5)$ w%), $\text{Bi}_7\text{F}_{11}\text{O}_5$ ($\sim 14.1(9)$ w%) and $\text{BiF}_{\sim 2.35}\text{O}_{\sim 0.9}$ ($\sim 4.2(6)$ w%), as confirmed by Rietveld refinements of synchrotron (Alba, MSPD, $\lambda = 0.4125$ Å) and neutron (ILL, D20, $\lambda = 1.542$ Å) powder diffraction data, see Fig.3a. Note that all the experiments using either single crystal, either powder have been performed from a unique batch, to avoid possible slight off-stoichiometry, while confronting our results.

The ^{57}Fe Mössbauer spectrum collected at room temperature using 20 mg of the sample is shown in Figure 3b. It was modeled with two paramagnetic components, *i.e.* quadrupole doublets (QD1 and QD2). The refined hyperfine parameters listed in Table S5, Supporting

Information, are characteristic of six-fold coordinated high spin Fe^{3+} (QD1) with $\delta_1 = 0.43(3)$ mm/s and $\Delta_1 = 0.48(5)$ mm/s and high spin Fe^{2+} in octahedral symmetry (QD2) with $\delta_2 = 1.29(3)$ mm/s and $\Delta_2 = 1.46(6)$ mm/s. Both isomer shift values ($\delta_1 > 0.4$ mm/s for Fe^{3+} and $\delta_2 > 1.2$ mm/s for Fe^{2+}) are consistent with relatively strong ionic Fe-F bonds^[20] and the relatively low value of the QD1 quadrupole splitting parameter ($\Delta_1 < 0.5$ mm/s) indicates that Fe^{3+} ions are located at a regular octahedral site, *i.e.* with moderate distortion. However, the broad line widths ($\Gamma > 0.4$ mm/s) suggest slightly disordered local environments for all Fe ions and/or crystallographic site distribution in terms of Fe – F bond lengths or distortions. The relative proportion QD1:QD2 was fitted to 59:41, but the absorption area of the Fe^{2+} doublet is likely underestimated due to non-equivalent Lamb-Mössbauer factors (f) for Fe^{2+} and Fe^{3+} at ambient temperature, such that a mixed $\text{Fe}^{\sim 2.5+}$ valence can be estimated, close to the structural $\text{Fe}^{\sim 2.6+}$ value deduced from our single crystal refinement after refining the Bi occupancy.

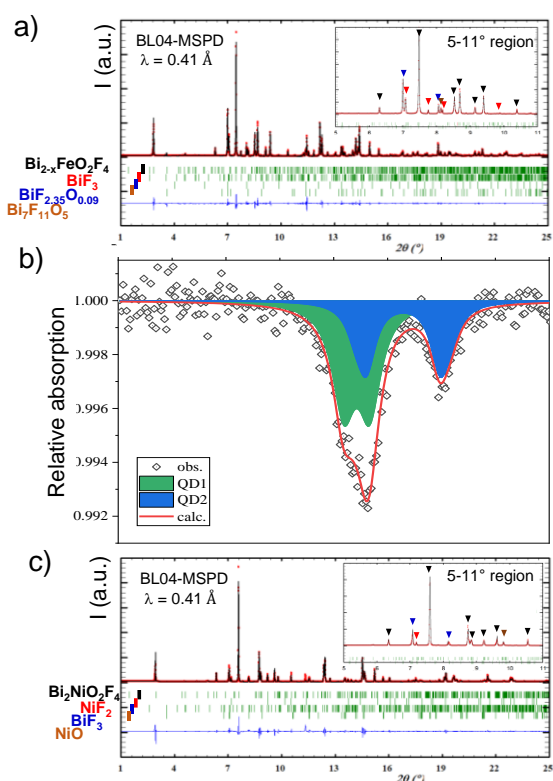


Figure 3: a) BiFeOF SXPDP Rietveld refinement with detail of the side-phases. The arrows in the inset are associated by color to the phases reported at the bottom. b) BiFeOF ^{57}Fe Mössbauer spectrum at 293 K fitted with QD1 and QD2 components and their sum (red line). c) BiNiOF Rietveld refinement of the synchrotron data.

After checking from our single-crystal model that the calculated b -doubling powder satellites are barely observable on both powder SXRPD and NPD data, we analyzed these data individually in the $P2_1ab$ average model ($a \sim 5.4 \text{ \AA}$, $b \sim 5.4 \text{ \AA}$, $c \sim 16.5 \text{ \AA}$), see Figure S2, Supporting Information. The refinement of the atomic coordinates is improved after refinement of Bi-occupancies ($\sim 91 \%$) leading $R_{Bragg} = 5.61\%$ (NPD data) and 7.82% (SRXRD data), comforting the bulk $(\text{Bi}_{1.8}\text{O}_2)(\text{FeF}_4)$ stoichiometry. However, slight stoichiometric between different batches cannot be excluded. NPD data also validated fully occupied anionic (O and F) positions, similarly to our single crystal data.

4. $(\text{Bi}_2\text{O}_2)(\text{NiF}_4)$ crystal structure

4.1 Rietveld refinement: Our best sample contains $66.5(7) \text{ w\%}$ of BiNiOF , $11.0(5) \text{ w\%}$ of NiF_2 , $11.5(5) \text{ w\%}$ of BiF_3 and $11.0(5) \text{ w\%}$ of NiO , see Fig.3c. We note that even if the ratio of impurity may change from a batch to another one, the XRD pattern of the title phase does not vary, which validate no deviation from the ideal stoichiometry determined here. Contrarily to the Fe case, the ideal stoichiometry $(\text{Bi}_2\text{O}_2)(\text{NiF}_4)$ is likely forced by the thermodynamic instability to oxidize Ni^{3+} species in a fluoride coordination ^[21]. The crystal structure of $(\text{Bi}_2\text{O}_2)(\text{NiF}_4)$ (*i.e.* BiNiOF) at room temperature was analyzed by Rietveld refinement starting from both the centrosymmetric (CS) $Pcab$ space group and the $P2_1ab$ model of the iron compound, see Figure S3, Supporting Information. The CS model was refuted due to higher R_{Bragg} ($= 6.03 \%$) and large thermal parameters for F atoms ($B_{iso} = 2.2 \text{ \AA}^2$) in the NPD. The non-centrosymmetric model was confirmed by qualitative SHG emission, see Fig. S1, Supporting information. It was optimally adjusted and refined in two steps using synchrotron data ($R_{Bragg} = 8.52 \%$) for accurate metal positions, and NPD data ($R_{Bragg} = 4.36 \%$) for further fine refinement of oxygen and fluorine positions. Selected distances and BVS are given in Table S6, S7, S8, Supporting Information. A tilt of the octahedra both in the ab plane and along c is observed, similarly to the iron compound, see Figure 2e Bi-O and Ni-F distances are in the $2.24 - 2.40 \text{ \AA}$ and $1.85 - 2.11 \text{ \AA}$ ranges respectively, giving BVS of $2.75 - 2.80$ and 2.10 for Bi^{3+} and Ni^{2+} ions respectively. Here again the BVS of F^- anions is ~ 1 , validating fluoride perovskite slabs. No deviation from the ideal $(\text{Bi}_2\text{O}_2)(\text{NiF}_4)$ formula was refined on all cations and anions. Analyzing the relationship between our $Pcab$ and $P2_1ab$ solutions using *Isodistort* indicates that from the two active modes Γ^{1+} and Γ^{3-} only the Γ^{3-x} component creates a significant but weak polar displacement along the a -axis for all atoms.

4.2 Structural modulations: For BiNiOF, the [110] ED pattern also reveals weak spots compatible with a modulation vector $q = (1/2a^*, 1/2b^*, 0)$. This is different from what has been observed in BiFeOF, but similar to what observed for the Co compound, prepared in the frame of this work as described in [10]. Here the modulation is incommensurate as defined by $q = (0.48a^*, 0.48b^*, 0)$, see blue arrows on Figures 1f and 1g. The origin of such phenomena is not well understood yet, but may picture displacive phenomena similar to the iron case, but with poor coherence in the polycrystalline sample, as it was not observed by NPD nor X-ray powder diffraction. The main crystallographic data for the series are listed in the Table 1 together with the magnetic features discussed later. Crystallographic data associated to CCDC numbers 2154827 and 2154840 can be download free from the FIZ Karlsruhe, Germany, <http://www.fiz-karlsruhe.de/>.

Table 1: Crystallographic and magnetic parameters for the $(\text{Bi}_2\text{O}_2)(\text{MF}_4)$ series

$(\text{Bi}_{1.8}\text{O}_2)(\text{FeF}_4)$	$(\text{Bi}_2\text{O}_2)(\text{CoF}_4)$ ^[10]	$(\text{Bi}_2\text{O}_2)(\text{NiF}_4)$
Unit cell dimension		
$r(\text{Fe}^{2+/3+})^{\text{VI}} = 0.78/0.65 \text{ \AA}$	$r(\text{Co}^{2+})^{\text{VI}} = 0.74 \text{ \AA}$	$r(\text{Ni}^{2+})^{\text{VI}} = 0.69 \text{ \AA}$
$a = 5.433(1) \text{ \AA}$	$a = 5.435(3) \text{ \AA}$	$a = 5.4048(1) \text{ \AA}$
$b = 5.431(1) \text{ \AA}$	$b = 5.435(3) \text{ \AA}$	$b = 5.4125(1) \text{ \AA}$
$c = 16.577(3) \text{ \AA}$	$c = 16.341(8) \text{ \AA}$	$c = 16.0522(3) \text{ \AA}$
$V = 489.13 \text{ \AA}^3$	$V = 482.66 \text{ \AA}^3$	$V = 469.58 \text{ \AA}^3$
Space group / struct. modulations		
$P2_1ab$	$P2_1ab$ supposed	$P2_1ab$
$0 \frac{1}{2} 0$ (SG: $P2_1I1$)	$\frac{1}{2} \frac{1}{2} 0$ (<i>this work</i>)	$0.48 \ 0.48 \ 0$
paramagnetism		
$\mu_{\text{eff}} = 5.52 \mu_{\text{B}}/\text{Fe},$ $\theta_{\text{CW}} = -338 \text{ K}$	$\mu_{\text{eff}} = 5.62 \mu_{\text{B}}/\text{Co},$ $\theta_{\text{CW}} = -142 \text{ K}$	not determined due to magn. impurities
Magnetic ordering		
$T_N = 89 \text{ K}, k = [0 \ 0 \ 0]$	$T_N = 50 \text{ K}$	$T_N = 45 \text{ K}, k = [0 \ 0 \ 0]$
$M_{\text{Fe}} = 4.2(1) \mu_{\text{B}}$	<i>not reported</i>	$M_{\text{Ni}} = 1.3(8) \mu_{\text{B}}$
$J_{\text{intra}} = +33.8 \text{ K. K}_b$ (DFT+U)	-	$J_{\text{intra}} = +54.7 \text{ K. K}_b$
$J_{\text{inter}} = -2.91 \text{ K. K}_b$	-	$J_{\text{inter}} = +0.03 \text{ K. K}_b$

4. $(\text{Bi}_2\text{O}_2)(\text{FeF}_4)$ Electronic Structure

Due to the multiple combination of individual anionic features, mixed anionic compounds offer a playground for band gap engineering, redox tuning etc... ^[22] such that the examination of the density of states (DOS) of fully O/F ordered Aurivillius oxyfluorides is relevant. It was calculated for the ideal $\text{Bi}_2\text{FeO}_2\text{F}_4$ compound, using DFT + U (U= 5 eV) in a spin-polarized ferromagnetic configuration, see Figure 4. Focusing on the top-block of the valence band (VB)

between -7 eV and E_F , the mixed Bi-O states occur below -2.7 eV, with a sharpest Bi $6p$ and $6s$ mixed states at the top, which emphasize the standard lone-pair stereoactivity, similarly to what is found in *Aurivillius* oxides such as $(\text{Bi}_2\text{O}_2)(\text{WO}_4)$ [23]. However, the existence of partially d -filled Fe^{2+} levels in the perovskite slabs drastically modifies the main metal-contribution at the top of VB. One can distinguish two main domains. The π^* Fe – F bonding with d - t_{2g} states extent up to -2.7 eV in a very delocalized band, composed by F – p states and Fe – d states, and are mixed with the Bi/O states, due to the chemical O – Bi – F – Fe bridges by apical F positions. The DOS at the top of the VB (-2.7 eV to E_F) is relatively well separated from the lower manifold and formed exclusively of the axial Fe – F overlaps characterized by sharp π^* states between the Fe e_g and F p orbitals. The on-site repulsion U shifts the down electrons (\downarrow) and mixed F – p states to the Fermi level. The calculated bandgap is 0.82 eV between E_F and the bottom of the conduction band (CB) exclusively formed of empty Bi, F and O states, while the first Fe – d down states grow at 3.6 eV. This hampers any Fe – Fe electronic hopping through the F shared corners, in good agreement with the checked experimental impossibility to measure a reasonable conductivity on a densified pellet. The strong electronegativity of fluor, leads to the general trends for F – p states below the O – p states, such as in LiFeSO_4F [24] and is responsible for the higher redox potential in oxyfluorides lithium cathodes. This behavior is especially pronounced in most of the reported layered perovskite oxyfluorides, $\text{Ba}_5\text{Co}_5\text{FO}_{13}$, $\text{La}_{1.2}\text{Sr}_{1.8}\text{Mn}_2\text{O}_3\text{F}$, $\text{La}_{1.2}\text{Sr}_{1.8}\text{Mn}_2\text{O}_3\text{F}_2$, $\text{Sr}_3\text{Ru}_2\text{O}_7\text{F}_2$, $\text{Sr}_2\text{FeO}_3\text{F}$, $\text{Sr}_3\text{Fe}_2\text{O}_4\text{F}_4$, $\text{Ba}_2\text{PdO}_2\text{F}_2$ where F⁻ and alkali-earth are confined in ionic spacers [25,26]. However, in our *Aurivillius* phases a singular situation appears where the covalent Fe – F bonds shift the F_{2p} states up to the top of the VB, much above the O_{2p} which interact with Bi states.

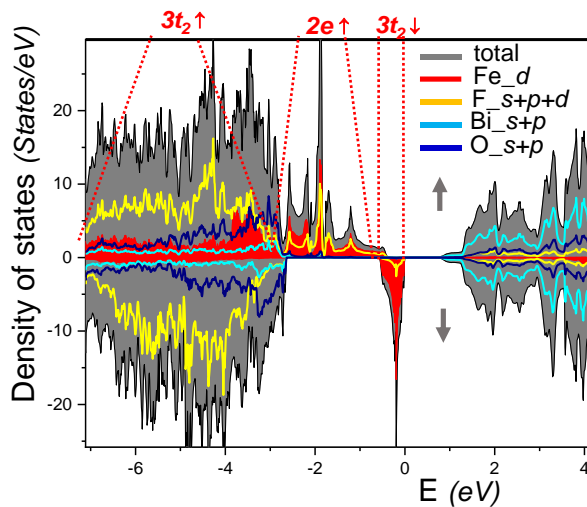


Figure 4 : Total and atomic resolved projected DFT+U ($U=5$ eV) DOS for $(\text{Bi}_2\text{O}_2)(\text{FeF}_4)$ (ferromagnetic spin polarized configuration).

5. Magnetism (M=Fe, Ni)

5.1 Magnetic properties: The thermal evolution of the direct and inverse magnetic susceptibilities χ (assumed from M/H) and χ^{-1} in zero field cooled (ZFC) and field cooled (FC) conditions after correction from diamagnetic impurities are displayed in Fig. 5a,d for BiFeOF and BiNiOF. Above 150 K, BiFeOF shows a paramagnetic behavior fitted to a Curie-Weiss law ($\mu_{eff} = 5.52(5) \mu_B/Fe$ and $\theta_{CW} = -338(1) K$), very close to what expected for mixed valent $Fe^{2.5+}$ in a spin-only approximation, $\mu_{exp} = 5.43 \mu_B/Fe$. Therefore, the orbital contribution for Fe^{2+} ($L = 2$) seems nearly quenched, in contrast with what is observed in most Fe^{2+} minerals [27]. Around 125 K, $\chi(T)$ increases and a ZFC/FC divergence occurs at $T_N \approx 89 K$, which denotes a canted AFM ordering. Below T_N , hysteresis loops are observed in $M(H)$ plots. At 2 K a remnant moment of $0.05 \mu_B/Fe$ is superposed to the AFM linear $M(H)$ evolution, see Fig 5c. Although no clear λ -type anomaly was evidenced in the specific heat data $C_p(T)$, a clear change is visible at T_N when plotting $C_p/T(T)$, together with a divergence between the zero-field and 1T data, see Figure 5b. Most plausibly, this behavior signs low-dimensional correlations in the perovskite slabs, prior to the Néel transition. Due to significant amount of impurities, ~ 18 wt.% of bismuth oxofluoride, no attempt to extract the magnetic entropy was pursued. However, DFT calculations of the main exchange interactions J_{intra} (between next neighbors in plane) and J_{inter} (across the $[Bi_2O_2]$ gap), validate robust 2D antiferromagnetic correlations in the perovskite slabs. DFT + U calculations ($U = 5$ eV, well adapted to the magnetism of $BaFe_2(PO_4)_2$ [28]), returns $J_{intra}/K_b = +33.81 K$ and $J_{inter}/K_b = -2.91 K$ for stoichiometric BiFeOF. Note that in the $P2_1ab$ subcell, J_{intra} are split along two directions $J_{(110)}$ and $J_{(1-10)}$ which are inequivalent but considered similar due to the negligible orthorhombic distortion. Using a mean-field (MF) approximation in the perovskite slabs for $\theta_{CW} = zJS(S+1)/3k_B$, where $z = 4$ is the average number of neighboring Fe spins, results in $|\theta_{CW}| = 270 K$ and $394 K$ for Fe^{2+} and Fe^{3+} respectively, averaging to a $332 K$ value that matches well our experimental value of $338(1) K$. We found for BiNiOF $J_{intra}/K_b = +54.67 K$ and $J_{inter}/K_b = +0.032 K$. The increase of J_{intra} compared to BiFeOF results from the in-plane lattice contraction, while across the interlayer gap the magnetic connection is hampered by the electron pairing in the t_{2g} states in $d^8 Ni^{2+}$, in contrast to $d^6 Fe^{2+}$.

Comparison between T_N values in the $Fe^{2.5+}$, Co^{2+} , Ni^{2+} series shows a direct scaling by the spin values. In the nickel analogue, the presence of paramagnetic impurities did not allow the determination of accurate Curie-Weiss parameters, but the thermal evolution of the PND

magnetic contribution data indicates $T_N \sim 45$ K, see Figure 5f. At this temperature, we also observe the increase of the $M(H)$ coercivity due to the contribution of canted-spins in both NiF_2 ($T_N = 68.5$ K [29]) and $(\text{BiO}_2)(\text{NiF}_4)$, see Figures 5e, and S4, Supporting Information. For $(\text{Bi}_2\text{O}_2)(\text{CoF}_4)$, in between BiFeOF and BiNiOF , an intermediate value $T_N \sim 50$ K was reported [10].

Besides the 2D-Ising exception, no long-range order (LRO) above zero temperature can be expected for genuine 2D systems. However, very weak J_{inter} couplings lead to a finite Néel temperature. For weakly coupled 2D Heisenberg $S = 1/2$ and $S = 1$ antiferromagnets, the estimation of T_N has been analytically studied via $T_N = 4\pi \cdot n \cdot J_{\text{intra}} / [b - \ln(|J_{\text{inter}}/J_{\text{intra}}|)]$ using a modified random-phase approximation (RPA), where n and b were adjusted from various materials [30]. For $S = 5/2$ Fe^{3+} ions, a good estimation of T_N was achieved using $S = 1$ values ($n = 0.68$ and $b = 3.12$) [31]. For BiFeOF with mixed valent $\text{Fe}^{2.5+}$, the same n and b values result in a $T_N \sim 101$ K, slightly overestimated compared to the experimental $T_N = 89$ K. For BiNiOF , it returns an excellent estimation of $T_N = 44.2$ K compared to its experimental value of ~ 45 K.

Comparison between T_N values in the $\text{Fe}^{2.5+}$, Co^{2+} , Ni^{2+} series shows a direct scaling by the spin values. For $(\text{Bi}_2\text{O}_2)(\text{CoF}_4)$, in between BiFeOF and BiNiOF , an intermediate value $T_N \sim 50$ K was reported [10].

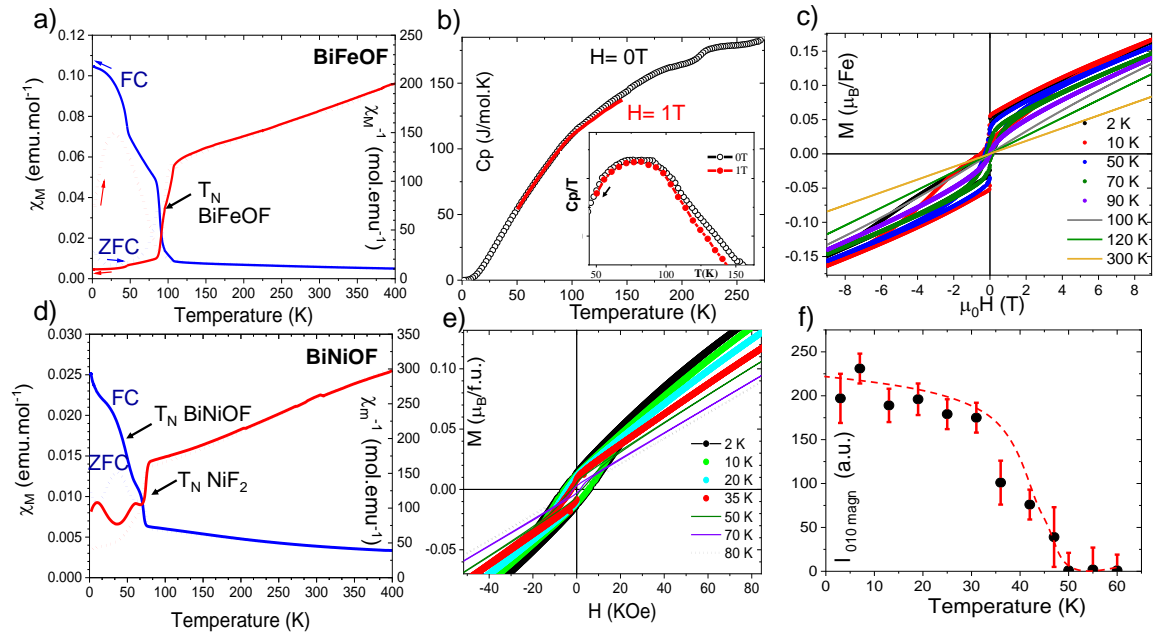


Figure 5 : BiFeOF : a) $\chi(T)$ and $\chi^{-1}(T)$ at $H=0.1$ T. b) $C_p(T)$ at 0T and 1T. c) $M(H)$ at various temperatures. BiNiOF : d) $\chi(T)$ and $\chi^{-1}(T)$ at $H=0.5$ T. e) $M(H)$ at various temperatures with weak ferrimagnetism. f) Intensity of the 010 magnetic contribution.

5.2 Magnetic Structures (M=Fe, Ni): The magnetic structures of $(\text{Bi}_{1.8}\text{O}_2)(\text{FeF}_4)$ and $(\text{Bi}_2\text{O}_2)(\text{NiF}_4)$ were solved and refined from NPD data collected at 1.5K on the D20 diffractometer ($\lambda = 2.41\text{\AA}$) and D1b ($\lambda = 2.52\text{\AA}$) respectively, at the Institut Laue Langevin (ILL), Grenoble, France, best adapted to the available amount of samples in each case. For both, we used the (a, b, c) sub-cell ($P2_1ab$ symmetry). For BiFeOF, the pattern difference 1.5K – 110K was used to remove all non-magnetic impurity contributions. In the BiNiOF case, due to the presence of NiF_2 ($T_N = 68.5\text{ K}$)^[29] and NiO ($T_N = 523\text{ K}$)^[32], the full pattern was fitted to consider both magnetic and crystallographic contributions for all phases using a single set of Pseudo-Voigt profile parameters for all nuclear and magnetic peaks, see Fig.6 a,b

In both cases, the magnetic contributions growing below T_N can be indexed with the magnetic propagation vector $k = [0, 0, 0]$ with conservation of the structural sub-cell for the magnetic periodicity. Magnetic symmetry analysis performed using Basireps^[33] indicates a decomposition of the Γ magnetic representation into 4 irreducible representations (Γ_{1-4}) of dimension 3. The best agreement for both compounds is following the Γ_1 representation ($R_{magn} = 22\%$ and 30% for Fe and Ni, respectively) with a spin-zero-component along the b -axis, see Table 2 and Figure 6. However, combining the Γ_4 irreducible representation for the y -component allows for a canted of spin structure bringing a possible M_y ferromagnetic component, experimentally observed in $M(H)$ plots ($M_{rem} = 0.05\ \mu_B$ in the Fe case). The refinement of such tiny spin deviation is out of our experimental resolution.

The magnetic moments at 1.5 K is refined at $4.2(1)\ \mu_B/\text{Fe}$ and $1.3(8)/\text{Ni}$, see Figure 6c, d. Despite the mixed $\text{Fe}^{2/3+}$ valence the iron moment is very close to what is found for FeF_2 ^[34] but much lower than in other layered Fe^{2+} oxide compound such as the 2D-Ising ferromagnetic $\text{BaFe}_2(\text{PO}_4)_2$ with $m_{\text{Fe}^{2+}} = 5.01\ \mu_B$ ^[28]. For $\text{Bi}_2\text{NiO}_2\text{F}_4$ the Ni value is similar to what is refined in the NiF_2 ^[35] side-phase, *i.e.* $1.35\ \mu_B/\text{Ni}$. In both compounds, the reduced moments from the expected $2S$ value plausibly stem from the 2D character of the perovskite slab and the strong F^- electronegativity. Indeed our DFT calculations show that apical F^- hold residual moments up to $0.04\ \mu_B$ and $0.06\ \mu_B$ for the Fe and Ni cases respectively.

Table 2 : Refined M_x, M_y, M_z according to the Γ_1 and the Γ_4 irreducible representation for the magnetic structures of $(\text{Bi}_2\text{O}_2)(\text{MF}_4)$ compounds.

Coord. TM	Γ_1 irr. Rep.	Γ_2 irr. Rep.	Γ_3 irr. Rep.	Γ_4 irr. Rep.	Refined Moment (μ_B)
x, y, z	M_x, M_y, M_z	M_x, M_y, M_z	M_x, M_y, M_z	M_x, M_y, M_z	M = Fe: $M_x = -3.17(2)$, $M_y = 0, M_z = 2.76(4)$ $M_{\text{total}} = 4.2(1)$
$x + \frac{1}{2}, -y, -z$	$M_x, -M_y, -M_z$	$M_x, -M_y, -M_z$	$-M_x, M_y, M_z$	$-M_x, M_y, M_z$	
$x, y + \frac{1}{2}, -z$	$-M_x, -M_y, M_z$	$M_x, M_y, -M_z$	$-M_x, -M_y, M_z$	$M_x, M_y, -M_z$	
					M = Ni: $M_x = -1.1(1)$,

$x+\frac{1}{2}, -y+\frac{1}{2}, z$	$-M_x, M_y, -M_z$	$M_x, -M_y, M_z$	$M_x, -M_y, M_z$	$-M_x, M_y, -M_z$	$M_y = 0, M_z = 0.7(2)$ $M_{\text{total}} = 1.3(8)$
------------------------------------	-------------------	------------------	------------------	-------------------	--

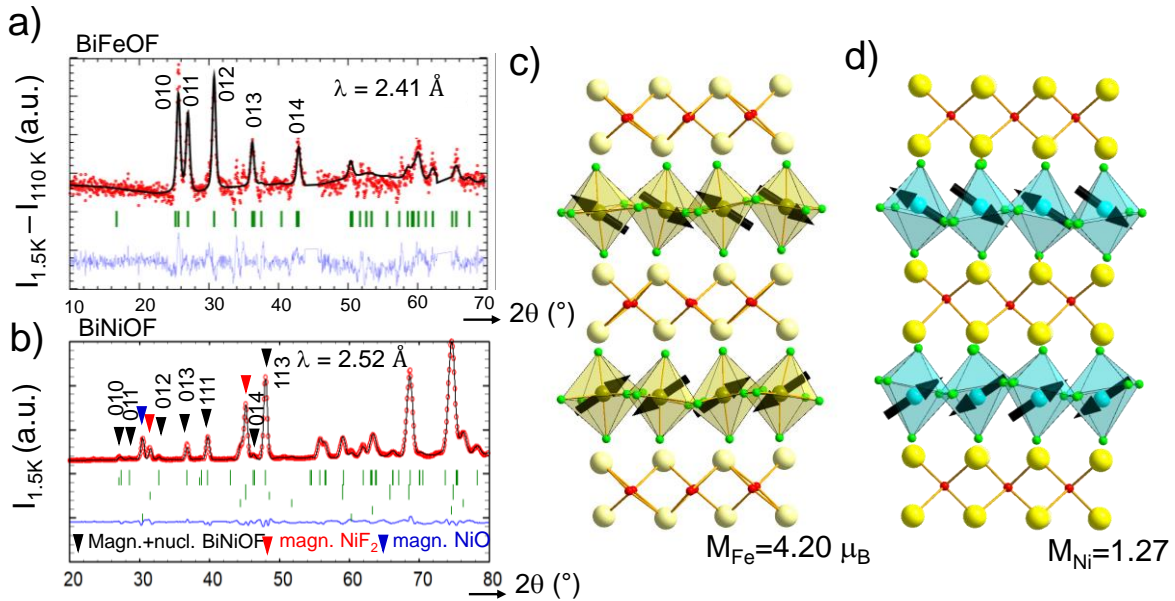


Figure 6 : Rietveld magnetic refinements at 1.5 K of a) BiFeOF (using difference pattern) and b) BiNiOF (using the full pattern). Magnetic maxima are marked. Refined magnetic structure for c) BiFeOF, d) BiNiOF.

6. Multiferroic properties of $(\text{Bi}_{1.8}\text{O}_2)(\text{FeF}_4)$

The relative scarcity of multiferroic magnetolectric was debated for long. It is based on the popular opinion that magnetism and ferroelectricity are mutually unlikely in oxides, especially perovskite-based ones, where the main ferroelectrics rely on d^0 electronic configurations and 2nd order Jahn-teller effect, while d^n orbitals are mandatory for magnetic order^[4]. However, this statement was re-adjusted based on the high number of ferroelectric (or assumed so) compounds found in nature including fluorides and oxyfluorides described in several review papers^[36,37]. Even though the strategy dealing with fluorine for oxygen substitution is well-identified and leads to: i) different hybridization properties due to their contrasted electronegativity and ii) the possible replacement of d^0 for d^n metals due to their different charges; experimental evidences of multiferroicity has only been proved for BaMF₄ family and tetragonal tungsten bronzes structures (TTB fluorides).^[38] Thus, the potentialities for magneto-electric couplings in layered oxyfluoride perovskite related compounds create a new paradigm in this field, investigate below.

6.1. Dielectric properties: Due to the contamination of our samples by side-phases, our dielectric properties have only been measured on the available $(\text{Bi}_{1.8}\text{O}_2)(\text{Fe}_2\text{F}_4)$ single crystals with electrical contacts in the ab plane. Here we consider a scenario where the mixed $\text{Fe}^{2+}/\text{Fe}^{3+}$

valence created by Bi sub-stoichiometry is detrimental to the intrinsic properties, increasing the dielectric losses. The thermal evolution of the capacitance at different magnetic fields is shown in Fig. 7a. It did not show significant field dependency apart a slight drift to lower values as increasing the field. However, a broad anomaly occurs at 230 K which is present in the heat capacity measurement $Cp(T)$ but not in the magnetic susceptibility and thus it suggests a structural origin, not investigated in the scope of this work. At T_N , the capacitance shows a broad maximum which suggests magneto-strictive origins as there are changes above and below the AFM transition. The poor effect of the magnetic field on the dielectric properties confirms the robust 2D-AFM exchanges. Indeed, between T_N and 150 K, $Cp(T)$ is affected by a magnetic field as low as 1 T, see Fig. 5b, the role of 2D magnetic correlations as deduced from our J calculations is plausibly crucial on the amplitude of the dielectric permittivity of $(\text{Bi}_{1.8}\text{O}_2)(\text{Fe}_2\text{F}_4)$ above T_N . In the current state, dealing within *in-plane* colinear structure, apart from the weak FM contribution, one would not expect any spin-induced ferroelectricity.

6.2. Ferroelectric properties: Next, we address the effect of the polar structure on the electric polarization calculated for the “*ideal*” stoichiometric $(\text{Bi}_2\text{O}_2)(\text{FeF}_4)$ in the average sub-cell giving rise to a polarization along a (P_x) between the paraelectric (P_{cab}) and the polar ($P_{2,ab}$) space groups. Both models were relaxed by DFT, constraining identical lattice parameters. The polarization was calculated using the Born Effective Charges (BECs) ^[39] computed using DFT for the paraelectric form and the atomic displacements, as detailed for $(\text{Bi}_2\text{O}_2)(\text{WO}_4)$ ^[40]. BECs tensors are reported in Table S8, S9s, Supporting Information.

In the subcell, after DFT structural relaxation, the polar component (by the Γ^3_x mode component, see above) almost vanish leading to $P_x = 0.5 \mu\text{C}/\text{cm}^2$ for the iron compound. However, a similar calculation using our experimental super-cell model yields the much bigger $P_x = 9.11 \mu\text{C}/\text{cm}^2$ value with nearly equal participation from the $[\text{Bi}_2\text{O}_2]$ and $[\text{FeF}_4]$ sub-units. Experimentally, ferroelectric hysteresis loops were measured in a resin-embedded $(\text{Bi}_{1.8}\text{O}_2)(\text{Fe}_2\text{F}_4)$ single crystal ($\sim 20 \times \sim 20 \times \sim 5 \mu\text{m}^3$) contacted on two opposite faces in the ab plane. The extrinsic contributions, such as leakage current and interface to $P(E)$ loop was eliminated using Positive-Up Negative-Down (PUND) measurements, which extract only the intrinsic hysteresis component. Remanent polarization appears using a maximum voltage of about 100 V but in very irregular hysteresis loops. Above $V_{\text{max}} = 160$ V a clear polarization loop emerges with a maximum value of $12.4 \mu\text{C}/\text{cm}^2$ at 70 kV/cm at room temperature, plausibly spurred by current leakage due to the mixed $\text{Fe}^{2/3+}$ valence, see Fig.7b. These values

are in accordance with the calculated P_x value using the refined crystal structure. The main origin for the calculated polarization being the Bi lone-pair and the off-centering of the Fe atoms in the perovskite slabs along the a -axis in the $P2_1ab$ based structure. Applied voltages higher than 200 V resulted in arcs forming inside the resin.

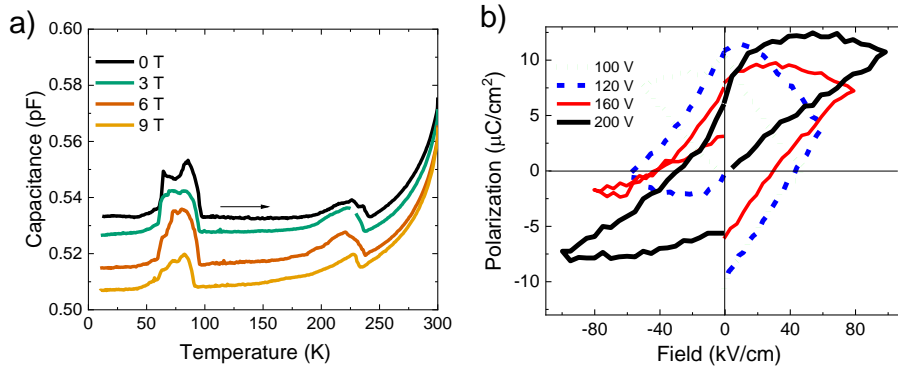


Figure 7: a) Capacitance as a function of the applied magnetic field and b) P(E) loop measured at several V max for a BiFeOF single crystal contacted in the (a,b) plane.

7. Concluding remarks.

The main research on *Aurivillius* multiferroics concern the $(\text{Bi}_2\text{O}_2)(\text{Ti}_3\text{O}_{10})$ modification of the pseudo-perovskite layers in the binary $(\text{Bi}_2\text{O}_2)(\text{Bi}_2\text{Ti}_3\text{O}_{10}) - \text{BiFeO}_3$ system^[41], leading to the $(\text{Bi}_2\text{O}_2)(\text{Bi}_{n-1}\text{Fe}_{n-3}\text{Ti}_3\text{O}_{3n+1})$ (BFTO- n) compounds. They combine ferroelectricity and magneto-electric coupling, where the origin of the former is a combination of oxygen octahedral rotations and polar distortions^[42,43]. The percolation necessary for magnetic long-range ordering in the perovskite slab was predicted to be $\sim 30\%$ of Fe/Ti^[44] substitution. However, it was only reached for blocks with thickness $n \geq 5$, *i.e.* in antiferromagnetic $(\text{Bi}_2\text{O}_2)(\text{Bi}_4\text{Ti}_3\text{Fe}_2\text{O}_{16})$, $(\text{Bi}_2\text{O}_2)(\text{Bi}_5\text{Ti}_3\text{Fe}_3\text{O}_{19})$, $(\text{Bi}_2\text{O}_2)(\text{Bi}_6\text{Ti}_3\text{Fe}_4\text{O}_{22})$ and $(\text{Bi}_2\text{O}_2)(\text{Bi}_7\text{Ti}_3\text{Fe}_5\text{O}_{25})$ ^[45-48], where the layered character is finally lost for a predominant perovskite character. Although weak intrinsic ferromagnetic component was proved by several techniques, including polarized neutrons reflectivity^[49], the segregation of Fe-rich areas into nano-domains, and other extrinsic contributions remains problematic with respect to the establishment of well-defined magnetic ordering and its coupling with dielectric properties. We report here the first example of “all Fe” and “all Ni” $n = 1$ *Aurivillius* phases, fully characterized, following the recent discovery of the cobalt analog. The divalent nature of the transition metals is forced by the incorporation of fluorides anions that solely occupy the (MF_4) perovskite sub-units. Despite, the plausible prediction of mixed metal valence due to mixed O/F occupancies, we show that in the iron case,

such valence occurs, but due to Bi-deficiency. All together our results open a wide prospective research area expanding the $n = 1$ type to larger ($n > 1$) “all magnetic” perovskite blocks, by sizeable O/F and Bi-vacancies. So far, such relevant *Aurivillius* mixed oxyfluorides have been prepared with diamagnetic ions metal ions as discussed in the introduction of this work. Of course in the recently reported $(\text{Bi}_2\text{O}_2)(\text{CoF}_4)$ compound ^[10], the ferroelectric properties are appealing. Indeed, we have demonstrated on $(\text{Bi}_{2-x}\text{O}_2)(\text{FeF}_4)$, the presence of both magnetic and electric ferroic orders and their coupling at T_N , giving clues for an extended series of novel multiferroic materials.

8. Experimental

$(\text{Bi}_2\text{O}_2)(\text{FeF}_4)$ was prepared through a hydrothermal route inspired by the synthesis of the cobalt analog ^[10]. A mixture of FeF_3 (1mmol) and Bi_2O_3 (1 mmol) together with 2.5 ml of deionized water and 0.5 ml of HF solution (7.65%) was sealed in a 23 ml Teflon lined steel autoclave, heated at 230 °C for 72 h and then cooled to room temperature. The products were washed with deionized water, followed by ethanol and left to dry in air at room temperature. Crystals (ideally brownish square-platelets, with maximal dimension 50 μm) were isolated for single-crystal characterization. For the analysis of polycrystalline samples, the best purity (~80%) was achieved after several sonication/separation cycles in ethanol to remove impurity loads, namely bismuth oxyfluorides as detailed below. Previous attempts to prepare $\text{Bi}_2\text{FeO}_2\text{F}_4$ compound via solid state reaction in vacuum sealed quartz ampoule heated up to 700 °C/72 h in standard or induction furnaces lead solely to a mixture of $\text{Bi}_7\text{F}_{11}\text{O}_5$, $\text{BiO}_{0.6}\text{F}_{1.66}$ and BiOF .

For $(\text{Bi}_2\text{O}_2)(\text{NiF}_4)$, the solubility of the NiF_2 precursor (40g/l @25°C) is much larger than for CoF_2 (0.14g/l @25°C) and FeF_3 (soluble in concentrated acidic conditions only), such that the hydrothermal reaction is displaced and led solely to bismuth oxyfluorides. Finally, NiF_2 was mixed to Bi_2O_3 , ground and pressed into pellets and introduced into platinum tubes. The best purity (~65%) was achieved after heating during 2 hours with intermediate grindings at 600 °C, 700 °C, 800 °C and 900 °C using a high frequency induction coil. The observed secondary phases are $\text{Bi}_7\text{F}_{11}\text{O}_5$, NiO and NiF_2 .

Single crystal data were collected on a Bruker X8 diffractometer (Ag-K_α radiation) and treated using the JANA 2000 suite ^[50]. Anticipating some weak disparities between different preparations, $(\text{Bi}_2\text{O}_2)(\text{FeF}_4)$ single crystals were selected from the same batch used throughout the bulk measurements reported below.

Powder XRD was carried out on a Cu-K α Bruker D8 Advanced diffractometer working on Bragg-Brentano geometry and high angular resolution synchrotron data collected on BL04 – MSPD ($\lambda=0.41$ Å) at ALBA, Barcelona/Spain).

Neutron powder diffraction (NPD) data have been collected on the D20 diffractometer of the Institut Laue Langevin (ILL), Grenoble/France at wavelength $\lambda = 1.542$ Å (high angular resolution mode) for the structural refinement and $\lambda = 2.41$ Å (high flux mode) for the magnetic structures. In the Ni case we also used the D1b diffractometer (and $\lambda = 2.52$ Å). The samples consist of powder set in vanadium cylinders.

Rietveld refinements were performed using the FULLPROF suite ^[51].

Magnetic characterization and heat capacities were obtained using a Quantum Design PPMS 9T DynaCool system.

DFT calculations were performed on the ideal (Bi₂O₂)(FeF₄) compound in its *P2₁ab* average cell using the projector augmented-wave (PAW) method ^[52,53] implemented in the Vienna ab initio simulation package (VASP) ^[53], with the full-potential local-orbital scheme (FPLO9.00-33) ^[54]. We used the generalized gradient approximation (GGA) for electron exchange and correlation corrections ^[55] applying the local density approximation (LDA + U, U = 5 eV). The cutoff energy for the plane wave expansion was 550 eV and reciprocal-space integration was performed on dense Monkhorst–Pack meshes ($8 \times 8 \times 3$). Convergence criteria of 10^{-6} and 10^{-4} were set for convergence of the electronic cycles and ionic relaxation respectively.

Electron diffraction study was performed on a FEI Technai G2-20 twin TEM microscope. The powder was crushed and dropped in the form of alcohol suspension on carbon supported copper grids followed by evaporation under ambient condition. Atomic resolved microscope images and EDS analysis were collected on a TEM FEI TITAN Themis 300, equipped with a probe corrector for resolution of 0.7 Å in STEM mode and a Super-X quad EDS detector for elemental analysis.

⁵⁷Fe Mössbauer experiment was performed with a constant acceleration Halder-type spectrometer operating in transmission geometry with a room temperature ⁵⁷Co(Rh) source (1.5 GBq). The Mössbauer spectrum of a thin absorber containing about 5 mg/cm² of Fe (⁵⁷Fe natural abundance 2.1 %) was recorded at room temperature and the refinement of the Mössbauer hyperfine parameters (δ isomer shift, Δ quadrupole splitting, Γ Lorentzian line width and relative areas) was performed using both homemade programs and the *WinNormos* ^[56] software. The ⁵⁷Fe isomer shifts are referenced to α -Fe⁰ at room temperature.

Second Harmonic Generation (SHG) signal was collected with 420-440 nm bandpass filter with excitation from femtosecond laser at 860 nm with 10% power and optical pathway modified

with quarter wave plate to have circular polarization. Images were acquired with a laser scanning microscope LSM 710 NLO (Carl ZEISS SAS, Marly le roi, France) coupled with CHAMELEON femtosecond Titanium-Sapphire Laser (Coherent, USA) and managed with ZEN Software (Carl ZEISS SAS, Marly le roi, France) with 10x objective lens.

The dielectric properties versus temperature were measured in a homemade-cell adapted to our PPMS-system, using a Keysight-E4980A LCR meter. P(E) loops were measured with the PUND technique on a RADIANT precision LC analyze equipped with a 4KV T-rek high voltage amplifier.

Acknowledgments

Emma Mc Cabe is thanked for fruitful discussion. Hiroshi Kageyama and the JSPS Core-to-Core Program (A) Advanced Research Networks (JPJSCCA20200004) are acknowledged for motivating this “anion mixed material research” study. The TEM facility in Lille (France) is supported by the Conseil Régional du Nord-Pas de Calais, and the European Regional Development Fund (ERDF). We thank ILL for the provision of beamtime on D20 and D1B (doi: 10.5291/ILL-DATA.EASY-849 and 10.5291/ILL-DATA.5-31-2775). CELLS-ALBA is acknowledged for beamtime on BL04-MSPD under proposal ID 2020094719. The Chevreul Institute (FR 2638), Region Hauts-de-France, and FEDER are acknowledged for funding the X-ray diffractometers and the PPMS magnetometer. We also thank C. Minaud for helping with the magnetic measurements and N. Djelal and L. Burylo for technical assistance.

Supplementary information:

SHG microscopy images – Rietveld refinement plots – M(H) Magnetization plots at various temperatures – Crystallographic Tables – Born effective charge tensors (DFT).

References:

- [1] Aurivillius, B., Mixed Bismuth Oxides with Layer Lattices. 1. The Structure Type of $\text{CaNb}_2\text{Bi}_2\text{O}_9$. *Ark. Kemi* **1949**, *1*, 463-480.
- [2] Vijatovic Petrovic, M. M.; Bobic, J. D. Perovskite and Aurivillius. In *Magnetic, Ferroelectric, and Multiferroic Metal Oxides*; Elsevier, 2018; pp 35–49. <https://doi.org/10.1016/B978-0-12-811180-2.00002-5>.
- [3] Megriche, A.; Lebrun, L.; Troccaz, M. Materials of $\text{Bi}_4\text{Ti}_3\text{O}_{12}$ Type for High Temperature Acoustic Piezo-Sensors. *Sensors Actuators A Phys.* **1999**, *78* (2–3), 88–91. [https://doi.org/10.1016/S0924-4247\(99\)00223-X](https://doi.org/10.1016/S0924-4247(99)00223-X).
- [4] Hill, N. A. Why Are There so Few Magnetic Ferroelectrics? *J. Phys. Chem. B* **2000**, *104* (29), 6694–6709. <https://doi.org/10.1021/jp000114x>.
- [5] Catalan, G.; Scott, J. F. Physics and Applications of Bismuth Ferrite. *Adv. Mater.* **2009**, *21* (24), 2463–2485. <https://doi.org/10.1002/adma.200802849>.

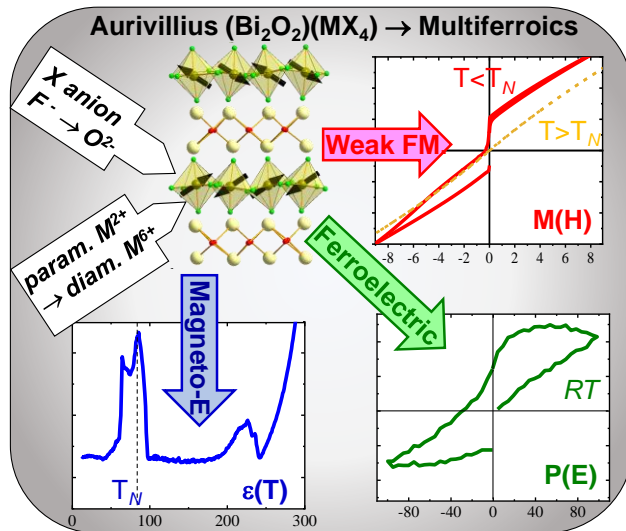
- [6] Jartych, E.; Pikula, T.; Mazurek, M.; Lisinska-Czekaj, A.; Czekaj, D.; Gaska, K.; Przewoznik, J.; Kapusta, C.; Surowie, Z. Antiferromagnetic Spin Glass-like Behavior in Sintered Multiferroic Aurivillius $\text{Bi}^{m+1}\text{Ti}_3\text{Fe}^{m-3}\text{O}_3^{m+3}$ Compounds. *J. Magn. Magn. Mater.* **2013**, *342*. <https://doi.org/10.1016/j.jmmm.2013.04.046>.
- [7] Kodama, H. Izumi, A., Watanabe, A., New Members of a Family of Layered Bismuth Compounds. *J. Solid State Chem.* **1981**, *36* (3), 349–355. [https://doi.org/10.1016/0022-4596\(81\)90446-1](https://doi.org/10.1016/0022-4596(81)90446-1)
- [8] Needs, R. L.; Dann, S. E.; Weller, M. T.; Cherryman, C.; Harris, R. The Structure and Oxide / Fluoride Ordering of the Ferroelectrics $\text{Bi}_2\text{TiO}_4\text{F}_2$. *J. Mater. Chem* **2005**, *15*, 2399–2407. <https://doi.org/10.1039/b502499d>.
- [9] Akopjan, A-V., Serov, T-V., Dolgikh, V-A., Ardaschnikovaa, E-I., Lightfoot, P. A new anion conductive bismuth–vanadium oxyfluoride. *J. Mater. Chem.*, **2002**, *12*, 1490–1494 DOI: [10.1039/b201049](https://doi.org/10.1039/b201049)
- [10] Mitoudi Vagourdi, E.; Müllner, S.; Lemmens, P.; Kremer, R. K.; Johnsson, M. Synthesis and Characterization of the Aurivillius Phase $\text{CoBi}_2\text{O}_2\text{F}_4$. *Inorg. Chem.* **2018**, *57* (15), 9115–9121. <https://doi.org/10.1021/acs.inorgchem.8b01118>.
- [11] McCabe, E. E.; Jones, I. P.; Zhang, D.; Hyatt, N. C.; Greaves, C. Crystal Structure and Electrical Characterisation of $\text{Bi}_2\text{NbO}_5\text{F}$: An Aurivillius Oxide Fluoride. *J. Mater. Chem.* **2007**, *17* (12). <https://doi.org/10.1039/b613970a>.
- [12] Ismailzade, I. H.; Ravez, J. $\text{Bi}_2\text{TiO}_4\text{F}_2$ – a New One-Layer Perovskite-like Ferroelectric. *Ferroelectrics* **1978**, *21* (1), 423–424. <https://doi.org/10.1080/00150197808237285>.
- [13] Giddings, A. T.; Scott, E. A. S.; Stennett, M. C.; Apperley, D. C.; Greaves, C.; Hyatt, N. C.; McCabe, E. E. Symmetry and the Role of the Anion Sublattice in Aurivillius Oxyfluoride $\text{Bi}_2\text{TiO}_4\text{F}_2$. *Inorg. Chem.* **2021**, *60* (18), 14105–14115., <https://doi.org/10.1021/acs.inorgchem.1c01933>
- [14] Benomar, S., Bousquet, E., Djani, H., Multianion induced out-of-plane proper polarization in oxyfluoride Aurivillius $\text{Bi}_2\text{TiO}_4\text{F}_2$, *J. Phys. Chem. Solids*, 2022, *167*, 110720. <https://doi.org/10.1016/j.jpcs.2022.110720>
- [15] Rae, A. D.; Thompson, J. G.; Withers, R. L. Structure Refinement of Commensurately Modulated Bismuth Tungstate, Bi_2WO_6 . *Acta Crystallogr. Sect. B Struct. Sci.* **1991**, *47* (6), 870–881. <https://doi.org/10.1107/S0108768191008030>.
- [16] van den Elzen, A. F.; Rieck, G. D. Redetermination of the Structure of Bi_2MoO_6 , Koechlinite. *Acta Crystallogr. Sect. B Struct. Crystallogr. Cryst. Chem.* **1973**, *29* (11), 2436–2438. <https://doi.org/10.1107/S0567740873006801>.
- [17] Theobald, F.; Laarif, A.; Hewat, A. W. The Structure of Koechlinite Bismuth Molybdate—a Controversy Resolved by Neutron Diffraction. *Ferroelectrics* 1984, *56* (1), 219–237. <https://doi.org/10.1080/00150198408221372>.
- [18] A.M. Glazer, The classification of tilted octahedra in perovskites, *Acta Cryst.* (1972). B28, 3384–3392. <https://doi-org/10.1107/S0567740872007976>

- [19] Zhang, Y.; Yamamoto, T.; Green, M. A.; Kageyama, H.; Ueda, Y. Interlayer Communication in Aurivillius Vanadate to Enable Defect Structures and Charge Ordering. *Inorg. Chem.* **2015**, *54* (22), 10925–10933. <https://doi-org/10.1021/acs.inorgchem.5b01964>
- [20] Gorev, M. V.; Flerov, I. N.; Tressaud, A.; Bogdanov, E. V.; Kartashev, A. V.; Bayukov, O. A.; Eremin, E. V.; Krylov, A. S. Heat Capacity and Magnetic Properties of Fluoride CsFe²⁺Fe³⁺F₆ with Defect Pyrochlore Structure. *J. Solid State Chem.* **2016**, *237*, 330–335. <https://doi.org/10.1016/j.jssc.2016.02.045>.
- [21] Zemva, B., Lutar, K., Chacdn, L., Fele-Beuermann, M., Allman, J., Shen, C., Bartlett, N., *J. Am. Chem. Soc.* **1995**, *117*, 10025-10034, Thermodynamically Unstable Fluorides of Nickel: NiF₄ and NiF₃ Syntheses and Some Properties, <https://doi.org/10.1021/ja00145a013>
- [22] Kageyama, H.; Hayashi, K.; Maeda, K.; Attfield, J. P.; Hiroi, Z.; Rondinelli, J. M.; Poeppelmeier, K. R. Expanding Frontiers in Materials Chemistry and Physics with Multiple Anions. *Nat. Commun.* **2018**, *9* (1), 772. <https://doi.org/10.1038/s41467-018-02838-4>.
- [23] Ait Ahsaine, H.; El Jaouhari, A.; Slassi, A.; Ezahri, M.; Benlhachemi, A.; Bakiz, B.; Guinneton, F.; Gavarri, J. R. Electronic Band Structure and Visible-Light Photocatalytic Activity of Bi₂WO₆: Elucidating the Effect of Lutetium Doping. *RSC Adv.* **2016**, *6* (103). <https://doi.org/10.1039/c6ra22669h>.
- [24] Chung, S. C.; Barpanda, P.; Nishimura, S.; Yamada, Y.; Yamada, A. Polymorphs of LiFeSO₄F as Cathode Materials for Lithium Ion Batteries – a First Principle Computational Study. *Phys. Chem. Chem. Phys.* **2012**, *14* (24), 8678. <https://doi.org/10.1039/c2cp40489c>.
- [25] Ehora, G.; Daviero-Minaud, S.; Colmont, M.; André, G.; Mentré, O. Ba₂Co₉O₁₄: New Inorganic Building Blocks with Magnetic Ordering through Super-Super Exchanges Only. *Chem. Mater.* **2007**, *19* (9). <https://doi.org/10.1021/cm062897q>.
- [26] Tsujimoto, Y.; Yamaura, K.; Takayama-Muromachi, E. Oxyfluoride Chemistry of Layered Perovskite Compounds. *Appl. Sci.* **2012**, *2* (1), 206–219. <https://doi.org/10.3390/app2010206>.
- [27] G. A. Parks, G.A., Akhtar, S. Magnetic moment of Fe²⁺ in paramagnetic minerals, *Am. Mineralogist.* **1968**, *53*, 406-415.
- [28] Kabbour, H.; David, R.; Pautrat, A.; Koo, H. J.; Whangbo, M. H.; André, G.; Mentré, O. A Genuine Two-Dimensional Ising Ferromagnet with Magnetically Driven Re-Entrant Transition. *Angew. Chemie - Int. Ed.* **2012**, *51* (47), 11745–11749. <https://doi.org/10.1002/anie.201205843>.
- [29] Arumugam, S.; Sivaprakash, P.; Dixit, A.; Chaurasiya, R.; Govindaraj, L.; Sathiskumar, M.; Chatterjee, S.; Suryanarayanan, R. Complex Magnetic Structure and Magnetocapacitance Response in a Non-Oxide NiF₂ System. *Sci. Rep.* **2019**, *9* (1), 3200. <https://doi.org/10.1038/s41598-019-39083-8>.

- [30] Yasuda, C.; Todo, S.; Hukushima, K.; Alet, F.; Keller, M.; Troyer, M.; Takayama, H. Néel Temperature of Quasi-Low-Dimensional Heisenberg Antiferromagnets. *Phys. Rev. Lett.* **2005**, *94* (21), 217201. <https://doi.org/10.1103/PhysRevLett.94.217201>.
- [31] Yang, H.; Mentré, O.; Zhu, T.; Minaud, C.; Ritter, C.; Zhang, X.; Jin, Y.; Lü, M. Fragile Magnetic Ordering between Robust 2D-Ferrimagnets in the $A\text{Fe}_3(\text{SeO}_3)_2\text{F}_6$ ($A = \text{K}, \text{Rb}, \text{Cs}$) Series. *J. Mater. Chem. C* **2022**, *10* (6), 2139–2148. <https://doi.org/10.1039/D1TC05650F>.
- [32] Ressouche, E.; Kernavanois, N.; Regnault, L.-P.; Henry, J.-Y. Magnetic Structures of the Metal Monoxides NiO and CoO Re-Investigated by Spherical Neutron Polarimetry. *Phys. B Condens. Matter* **2006**, 385–386, 394–397. <https://doi.org/10.1016/j.physb.2006.05.082>.
- [33] The FullProf Team. (2014) Basireps.
Rodríguez Carvajal, J. (2014)
https://neutrons2.ornl.gov/conf/2014/magstr/docs/Tutorial_Magnetic_Structures.pdf
- [34] Litterst, F. J. Susceptibility of Non-Crystalline Ferromagnetic FeF_2 . *J. Phys. Lettres* **1975**, *36* (7–8), 197–199. <https://doi.org/10.1051/jphyslet:01975003607-8019700>.
- [35] Erickson, R. A. Neutron Diffraction Studies of Antiferromagnetism in Manganous Fluoride and Some Isomorphous Compounds. *Phys. Rev.* **1953**, *90* (5), 779–785. <https://doi.org/10.1103/PhysRev.90.779>.
- [36] Ravez, J. The Inorganic Fluoride and Oxyfluoride Ferroelectrics. *J. Phys. III* **1997**, *7* (6), 1129–1144. <https://doi.org/10.1051/jp3:1997175>.
- [37] Scott, J. F.; Blinc, R. Multiferroic Magnetoelectric Fluorides: Why Are There so Many Magnetic Ferroelectrics? *J. Phys. Condens. Matter* **2011**, *23* (11), 113202. <https://doi.org/10.1088/0953-8984/23/11/113202>.
- [38] G. Calestani, F. Mezzadri, In *Photonic and Electronic Properties of Fluoride Materials*, Elsevier, **2016**, 285.
- [39] Ghosez, P.; Michenaud, J.; Gonze, X. Dynamical Atomic Charges: The Case of Compounds. *Phys. Rev. B - Condens. Matter Mater. Phys.* **1998**, *58* (10). <https://doi.org/10.1103/PhysRevB.58.6224>.
- [40] Djani, H.; Bousquet, E.; Kellou, A.; Ghosez, P. First-Principles Study of the Ferroelectric Aurivillius Phase Bi_2WO_6 . *Phys. Rev. B - Condens. Matter Mater. Phys.* **2012**, *86* (5). <https://doi.org/10.1103/PhysRevB.86.054107>.
- [41] Algueró, M.; Pérez-Cerdán, M.; del Real, R. P.; Ricote, J.; Castro, A. Novel Aurivillius $\text{Bi}_4\text{Ti}_{3-2x}\text{Nb}_x\text{Fe}_x\text{O}_{12}$ Phases with Increasing Magnetic-Cation Fraction until Percolation: A Novel Approach for Room Temperature Multiferroism. *J. Mater. Chem. C* **2020**, *8* (36), 12457–12469. <https://doi.org/10.1039/D0TC03210G>.
- [42] Algueró, M.; Sanz-Mateo, J.; del Real, R. P.; Ricote, J.; Fernández-Posada, C. M.; Castro, A. Multiferroic Aurivillius $\text{Bi}_4\text{Ti}_{2-x}\text{Mn}_x\text{Fe}_{0.5}\text{Nb}_{0.5}\text{O}_{12}$ ($n = 3$) Compounds with Tailored Magnetic Interactions. *Dalt. Trans.* **2021**, *50* (46), 17062–17074. <https://doi.org/10.1039/D1DT02220B>.

- [43] Sun, S.; Yin, X. Progress and Perspectives on Aurivillius-Type Layered Ferroelectric Oxides in Binary Bi₄Ti₃O₁₂-BiFeO₃ System for Multifunctional Applications. *Crystals* **2021**, *11* (1), 23. <https://doi.org/10.3390/cryst11010023>.
- [44] Kurzawski, L.; Malarz, K. Simple Cubic Random-Site Percolation Thresholds for Complex Neighbourhoods. *Reports Math. Phys.* **2012**, *70* (2), 163–169. [https://doi.org/10.1016/S0034-4877\(12\)60036-6](https://doi.org/10.1016/S0034-4877(12)60036-6).
- [45] Srinivas, A.; Suryanarayana, S. V.; Kumar, G. S.; Kumar, M. M. Magnetoelectric Measurements on And. *J. Phys. Condens. Matter* **1999**, *11* (16), 3335–3340. <https://doi.org/10.1088/0953-8984/11/16/014>.
- [46] Srinivas, A.; Kumar, M. M.; Suryanarayana, S. V.; Bhimasankaram, T. Investigation of Dielectric and Magnetic Nature of Bi₇Fe₃Ti₃O₂₁. *Mater. Res. Bull.* **1999**, *34* (6), 989–996. [https://doi.org/10.1016/S0025-5408\(99\)00093-8](https://doi.org/10.1016/S0025-5408(99)00093-8).
- [47] Srinivas, A.; Kim, D.-W.; Hong, K. S.; Suryanarayana, S. V. Study of Magnetic and Magnetoelectric Measurements in Bismuth Iron Titanate Ceramic—Bi₈Fe₄Ti₃O₂₄. *Mater. Res. Bull.* **2004**, *39* (1), 55–61. <https://doi.org/10.1016/j.materresbull.2003.09.028>.
- [48] Lomanova, N. A.; Morozov, M. I.; Ugolkov, V. L.; Gusarov, V. V. Properties of Aurivillius Phases in the Bi₄Ti₃O₁₂-BiFeO₃ System. *Inorg. Mater.* **2006**, *42* (2), 189–195. <https://doi.org/10.1134/S0020168506020142>.
- [49] Zhai, X.; Grutter, A. J.; Yun, Y.; Cui, Z.; Lu, Y. Weak Magnetism of Aurivillius-Type Multiferroic Thin Films Probed by Polarized Neutron Reflectivity. *Phys. Rev. Mater.* **2018**, *2* (4), 044405. <https://doi.org/10.1103/PhysRevMaterials.2.044405>.
- [50] V. Petříček, M. Dušek, L. Palatinus, Crystallographic Computing System JANA2006: General features. *Zeitschrift Für Kristallographie - Crystalline Materials*, **2014**, *229*, 345-352. DOI:[10.1515/zkri-2014-1737](https://doi.org/10.1515/zkri-2014-1737)
- [51] Rodríguez-Carvajal, J. Recent Advances in Magnetic Structure Determination by Neutron Powder Diffraction. *Phys. B Phys. Condens. Matter* **1993**, *192* (1–2), 55–69. [https://doi.org/10.1016/0921-4526\(93\)90108-I](https://doi.org/10.1016/0921-4526(93)90108-I).
- [52] Blöchl, P. E. Projector Augmented-Wave Method. *Phys. Rev. B* **1994**, *50* (24), 17953–17979. <https://doi.org/10.1103/PhysRevB.50.17953>.
- [53] Koepnik, K.; Eschrig, H. Full-Potential Nonorthogonal Local-Orbital Minimum-Basis Band-Structure Scheme. *Phys. Rev. B* **1999**, *59* (3), 1743–1757. <https://doi.org/10.1103/PhysRevB.59.1743>.
- [54] Kresse, G.; Hafner, J. Ab Initio Molecular Dynamics for Liquid Metals. *Phys. Rev. B* **1993**, *47* (1), 558–561. <https://doi.org/10.1103/PhysRevB.47.558>
- [55] Perdew, J. P.; Burke, K.; Ernzerhof, M. Generalized Gradient Approximation Made Simple. *Phys. Rev. Lett.* **1996**, *77* (18), 3865–3868. <https://doi.org/10.1103/PhysRevLett.77.3865>.
- [56] WinNormos-for-Igor Software Package; WaveMetrics Inc., 2008. Wissenschaftliche Elektronik GmbH

For Table of Content only



Synopsis :

The search for *Aurivillius*-based magnetoelectric multiferroics requests the incorporation of a maximal concentration of paramagnetic ions in the perovskite sub-units. This goal is partially achieved in the $\text{BiFeO}_3\text{-Bi}_4\text{Ti}_3\text{O}_{12}$ phase diagram, increasing the thickness of the perovskite slab until the magnetic percolation is reached ($\text{Fe}/(\text{Fe}+\text{Ti}) \sim 30\%$). Based on the recent discovery of $(\text{Bi}_2\text{O}_2)(\text{CoF}_4)$ compound, we show here that the alternative F^- for O^{2-} replacement allows for full-magnetic layers ($\text{M}=\text{Fe}, \text{Ni}$) with evidence of multiferroism in the iron case.